Experimental Investigation of the Influence of Bedding Planes and Differential Stress on Microcrack Propagation in Shale Using X-Ray CT Scan

Neel Gupta · Brijes Mishra

Abstract In past couple of decades, scanning electron microscope and digital image correlation has been extensively used to investigate the microcrack propagation in rocks. Only recently, X-ray computed tomography (CT) scans were used for more detailed understanding of the physico-mechanical behavior of rock specimens. In current study, the deformational behavior of bedded Marcellus shale was studied through the changes in the geometry of microcracks. Quasi-static triaxial tests at three successive levels of differential stress were conducted on cylindrical-shaped shale specimens at a confining pressure of 6.89 MPa. Mineralogical analysis indicated the homogenous composition of specimen, however, triaxial tests resulted varying modulus of stiffness at similar confining pressure. The X-ray CT scanned images of specimens prior to the triaxial stress showed the significant density of pre-existing microcracks. During triaxial tests, the successive levels of differential stress influenced the geometry of pre-existing microcracks. The differential stress equivalent to 55% and 65% of the differential strength significantly closed the pre-existing microcracks. However,

differential stress equivalent to 70% of the differential strength increased the density of microcracks. The orientation of the bedding plane only influenced the direction of microcrack propagation. The perpendicular-bedded specimen experienced significant microcrack propagation in the axial direction, while the parallel-bedded specimen experienced significant increase in the aperture of microcracks.

Keywords Shale · Bedding planes · X-ray CT scan · Image analysis · Microcrack geometry · Pre-existing microcracks

1 Introduction

Bedding planes are naturally occurring discontinuities in sedimentary rocks. It represents the break in similar sediments deposition, shown through the difference in the lithology of adjacent beds (Campbell 1967), and cause anisotropy in the properties of rock mass (Kuila et al. 2011). An in-depth study of bedding planes in underground coalmines is lacking due to the uncertainty of location of bedding planes in sedimentary rocks (Peng 2015). The most common examples of bedding planes are weak laminations in shale and thinly interbedded sandstone and shale, also called "stack rock" (Murphy 2016). The bedded coal, rock-like shale appears massive but is highly laminated and

N. Gupta (✉) · B. Mishra
Department of Mining Engineering, West Virginia University, Mineral Resource Building, 201, 1347 Evansdale Drive, Morgantown, WV 26506-6070, USA
e-mail: negupta@mix.wvu.edu

B. Mishra
e-mail: brijes.mishra@mail.wvu.edu

weak along the bedding plane. Therefore, previously, the weak bedding planes in shale were considered as a primary reason of unexpected roof failures in underground coalmines (Mark and Molinda 2007).

In the field, the coalmine roof rating (CMRR) analyzes the influence of bedding planes on the roof stability (Molinda and Mark 1994). However, in the laboratory, bedding planes characteristics are determined through several direct and indirect tests on intact bedded-rock specimens (Wang et al.2013; Kallu and Pedram 2015). For example, direct shear test of bedded rock specimens, oriented perpendicular to the longitudinal axis, estimates the cohesion and friction angle of the bedding planes. While, uniaxial and triaxial laboratory tests provide the failure strength, and Mohr–coulomb analysis determines the cohesion and angle of internal friction of the failure plane, or inherent plane of weakness. In addition, the indirect tests, such as Brazilian and point load test estimates the indirect tensile and uniaxial strength of intact bedded specimens, respectively (Li et al. 2013; ASTM 2016). The uniaxial strength experiments on sedimentary rock specimens with different bedding orientations showed that the failure strength depends on the angle between direction of major principal stress and the inherent plane of weakness or bedding planes, as shown in Fig. 1. Morgan and Einstein (2014) performed the uniaxial compression tests on Opalinus shale with high-speed imagery. The experiments indicated that the orientation of the bedding planes influenced the initiation and coalescence of tensile cracks. As a result, the bedded shale exhibited least strength when oriented at 60° to the horizontal direction. In 1993, Martin presented the correlation between the results of axial stress–strain curve and acoustic emission (AE) activity, and differentiated the several stages of microcrack propagation, as shown in Fig. 2. Although these correlations qualitatively explained the distinct stages of microcrack propagation in brittle rocks, the quantification of geometry of microcracks, such as area, aperture and volume are still under-investigated.

Techniques, such as scanning electron microscope (SEM) and digital image correlation (DIC) are extremely powerful tools for the direct visualization and quantification of rock microstructure. In earlier studies, SEM was used to visualize microcracks at grain level (Sprunt and Brace 1974; Tapponnier and Brace 1976). However, the requirement of small size specimens limits the microstructure analysis of cylindrical shaped rock specimen with 2 inches diameter and 4 inches length. In addition, the specimen preparation for SEM through dry cutting and polishing also influences the natural microstructure of rock specimens. Similarly, DIC is a useful technique in developing displacement vectors strain maps. However, its application is limited to the surface of rock specimen, and its extension to the 3D tomograms, such as digital volume correlation is still in developing stage (Bay 2008). Therefore, in current research, authors used X-ray computed tomography (CT) technique to visualize and quantify the internal microstructure of rock specimens. The biggest advantage of X-ray CT over other techniques is the non-destructive specimen preparation for the scanning purposes.

Lately, X-ray CT scan was only useful for visualizing the internal microstructure. While, with the developing technology, the technique has significantly improved in extracting quantitative information from 3D images (Maire and Withers 2014). In recent years, X-ray computed tomography (CT) technique extensively solved engineering problems of fracture geometry, mineral phase, pore network and crystal sizes (Deng et al.2016). This micro-level imaging technique enables the direct visualization and quantification of microcracks (Koeberl et al. 2002; Fredrich et al. 2006). The application is also beneficial over valuable unique specimens, such as meteorites and fossils. Gnos et al. (2010) used X-ray tomography to gather the interior information of meteorite in non-destructive manner. The X-ray tomograms revealed the presence of shock melt associated vesicles with preferred orientation. Rowe et al. (2001) used high resolution X-ray tomography to analyze the archaeoraptor fossil from Early Cretaceous beds of China. The X-ray tomography imaged the fracture pattern and distribution of materials in the fossil. Sellars et al. (2003) applied the CT technique during triaxial stress application and studied the fracture development in cubic quartzite blocks. They also compared the results with numerical model predictions, which was used to predict fracture development in deep mine excavations. Lenoir et al. (2007) used the CT imaging technique to image the shear deformation of argillaceous rocks under triaxial compression. Their experimental research found that the isochoric deformation in rocks prevents the detection of shear strain localization in X-ray CT images. Jia, Chen and Jin (2014)
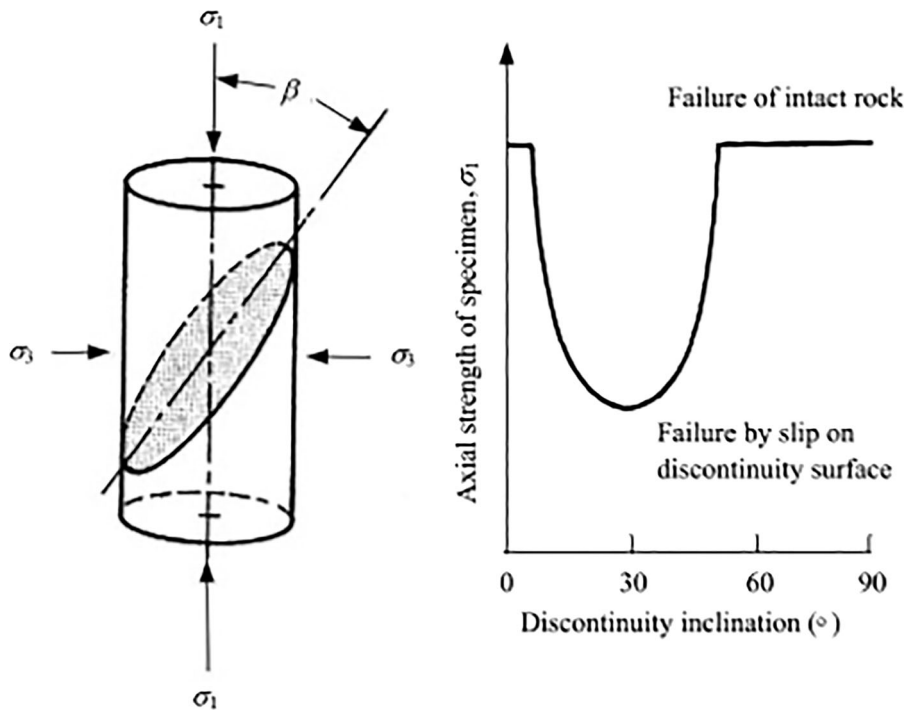
Fig. 1 Variation of axial strength with the orientation of discontinuity (Hoek and Brown 1980)
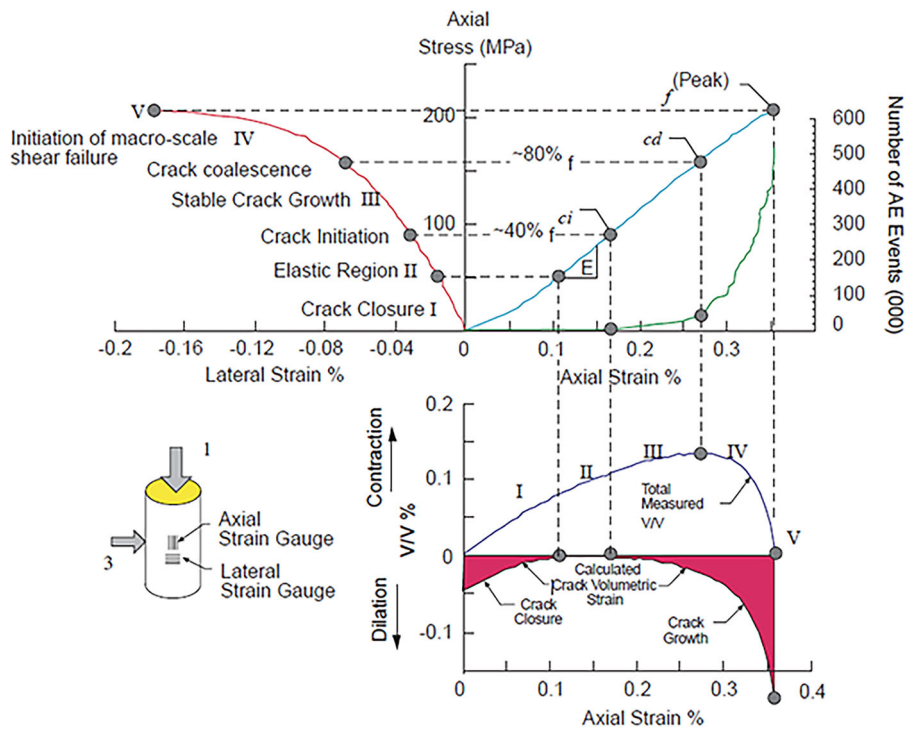

Fig. 2 Axial stress–strain diagram showing the different stages of crack development (Martin 1993)

used the X-ray CT technique for three-dimensional (3D) imaging of fractures in carbonate rocks. Yang et al. (2016) found crack propagations at high temperature through the X-ray CT scanner.

The objective of the current study is to determine the influence of orientation of bedding planes and pre-existing microcracks on the deformational behavior of Marcellus shale. The X-ray CT equipment scanned the cylindrical-shaped specimens before and after the conventional triaxial tests. The open-source image analysis software, FIJI (Schindelin et al. 2012) analyzed the X-ray CT images and determined the geometry of microcracks. The results of the change in the geometry of microcracks were qualitatively compared with the level of differential stress and perma-nent volumetric strain in the specimens. Although the current study of analyzing the changes in the geometry of microcracks is performed on Marcellus shale, the method is equally applicable on other types of sedimentary rocks. The term crack and microcrack were used synonymously in the paper. As the results of X-ray CT image processing depends upon the resolu-tion of CT images (Latief et al. 2017), in current research, only microcracks with aperture more than 29.9 microns were considered. The detailed descrip-tion about X-ray CT scanning and image processing are briefly explained in the methodology (Gupta 2019).

2 Methodology

Marcellus shale is the middle Devonian age unit of the ancient sedimentary system, also called as Appala-chian Basin (Popova 2017). It is an organic rich formation, extended in the subsurface from New York State in the North to Northeastern Kentucky and Tennessee in the South (Roen 1984) as shown in Fig. 3. According to the report of U.S. Energy Information Administration(Popova 2017), the pri-mary minerals of Marcellus shale are 9–35% mixed-layer clays, 10–60% quartz, 0–10% feldspar, 5–13% pyrite, 3–48% calcite, 0–10% dolomite, and 0–6% gypsum. Conventionally, the uniaxial compression strength of Marcellus shale varies between 26 and 99 MPa, such that the strength is maximum at 0° and 90° bedding orientations and minimum at approxi-mately 45°–75° (Cusatis et al. 2015). Based on the variation in sea level during deposition, it contains
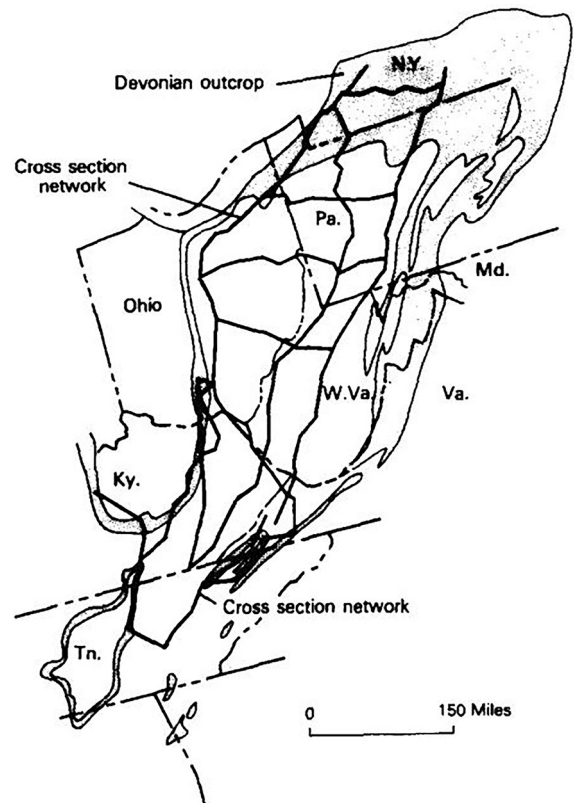

Fig. 3 Index map of stratigraphic cross-sections and the Devonian outcrop belt in the Appalachian Basin (Roen 1984)

shale with different colors and interbedded limestone. The color ranges from medium light gray to black, which provides information about the depositional environment. For example, Marcellus shale deposited in an oxygen-deficient environment is black with significant organic content. The elevation of Marcellus formation varies from 304.8 to − 2438.4 m subsea depth (Popova 2017).

In the current study, Marcellus shale specimens belonged to the Devonian outcrop in western New York. The specimens were light gray with no visible laminations. The coring direction of specimens was parallel and perpendicular to the bedding planes. The results of X-ray powdered diffraction (XRD) showed 75.14% calcite, 12.94% illite, 8.74% quartz and 3.18% pyrite (Gupta et al. 2018). The triaxial compression strength tests at four successive confining conditions showed variation in the failure strength of perpendic-ular and parallel bedded shale specimens. According to Niandou et al. (1997), the anisotropy degree of strength for transversely isotropic rocks is determined

by the ratio of failure strength in parallel and perpendicular bedding orientation (Eq. 1). Similarly, the coefficient of anisotropy (k) of Marcellus shale was determined at different confining stress states. The results are summarized in Table 1. The unit value of coefficient of anisotropy indicated negligible influence of the orientation of bedding planes on the peak strength of shale.

$$k = \frac{(\sigma_1 - \sigma_3)_\parallel}{(\sigma_1 - \sigma_3)_\perp}. \tag{1}$$

2.1 Constant Stress Rate Triaxial Test with X-Ray CT Scan

A generalized schematic of the Marcellus shale specimen with different types of bedding planes orientation is shown in Fig. 4a. While, the experimental procedure of constant stress rate triaxial test with X-ray CT scan is shown in Fig. 4b. Six shale specimens, bedded parallel (PL) and perpendicular (PD) to the orientation of longitudinal axis of the specimen were chosen for the constant stress rate triaxial test. The specimens were right cylindrical in shape, with both ends polished and grounded flat to maintain the ends parallel to 0.0013 mm. The diameter of shale specimen was 53.67 mm with length over diameter ratio greater than two (ASTM 2019). North-Star Imaging M-5000 Industrial CT equipment scanned each specimen and provided two-dimensional (2D) cross-sectional images. The X-ray CT scanned images of shale specimen before the triaxial test were termed as pre-triaxial stress state. As the level of applied stress was always significantly smaller than the failure strength, the specimens remained intact after unloading triaxial stress. The tested specimens were stored in a bubble wrap, and carefully taken back to the X-ray CT scanning facility to minimize the

influence of transportation on the internal microstructure of rock specimens.

The GCTS servo-controlled triaxial equipment applied the triaxial stress on the specimens, such that major principal stress (σ_1) is greater than the minor principal stresses [intermediate (σ_2) = minor principal stress (σ_3)]. The specimens were sealed inside the polyolefin jacket to prevent the contamination and absorption of oil on the surface pores and cracks in the specimen. Axial and radial linear variable differential transformers (LVDTs) mounted on the specimens recorded strain in the axial and radial directions, respectively. As the triaxial equipment did not directly measure the volumetric strain in the specimen, it was the arithmetic sum of axial strain and twice of radial strain. The procedure of the dry triaxial test involved two stages. In the first stage, the specimen was consolidated by increasing the axial and confining stress hydrostatically up to 6.89 MPa. Once the triaxial cell attained hydrostatic stress state, the confining stress remained constant and the axial stress was increased at the constant stress rate of 0.48 MPa/second up to the maximum value of differential stress smaller than the failure strength. In the second stage, the axial stress was removed at the constant rate of 0.48 MPa/second until the hydrostatic stress state of 6.89 MPa was reached. The intact shale specimens were retrieved after triaxial test and scanned again through Industrial X-ray CT equipment, termed as post-triaxial test state.

In the current triaxial test setup, three successive levels of differential stress were chosen, 55%, 65% and 70% of the differential strength, such that applied stress level might represent the stable growth of pre-existing microcracks, or nucleation of new microcracks. First, the average differential strength of shale at 6.89 MPa confining stress was determined through two triaxial strength tests on both parallel and perpendicular bedded specimens, mentioned in Table 2 (Gupta and Mishra 2017). The rate of increasing and decreasing axial stress was based on the ASTM Standards for the quasi-static triaxial test (ASTM 2014). In addition, the graph between volumetric strain and axial stress determined the level of yield and dilation stress, as shown in Fig. 5. According to Bieniawski (1967), the graph between axial stress and volumetric strain remains linear until the specimen reaches its yield strength (CI), while at dilation strength (CD) the volumetric strain is maximum in the

Table 1 Coefficient of anisotropy of Marcellus Shale (Gupta et al. 2018)

Confining stress (MPa)	Coefficient of anisotropy (k)
3.45	0.98
6.89	1.08
10.34	0.93
13.79	1.02

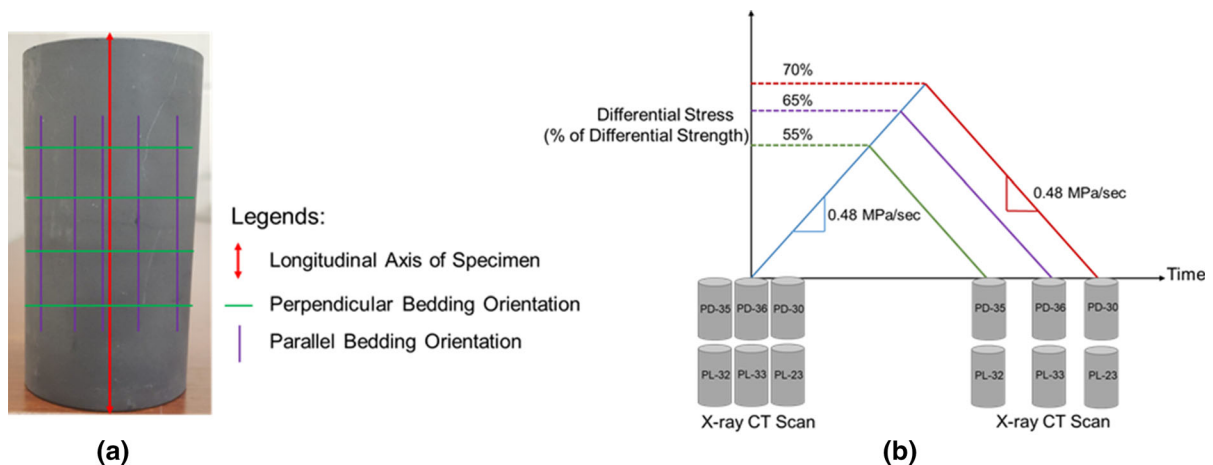**Fig. 4 a** Marcellus shale specimen with different bedding orientation; **b** Experimental procedure of constant stress rate triaxial tests with X-ray CT scan

Table 2 Average differential strength of Marcellus shale

Specimen ID	Confining stress (MPa)	Differential strength (MPa)	Average differential strength (MPa)	Yield stress (MPa)	Dilation stress (MPa)
PD-4	6.89	128.59	125.26	68.09	92.25
PD-6		121.93			
PL-6		136.7	135.84	55.92	104.13
PL-7		134.97			

direction of compression. According to Martin (1993), yield strength represents the initiation of microcracks, while dilation stress represents the propagation of unstable microcracks (Fig. 2).

2.2 X-Ray CT Scan of Cylindrical Shale Specimen

In the current study, North-Star Imaging (NSI) M-5000 Industrial CT scanner imaged the shale specimens. The resolution of this scanner depends on the size of the specimen, ranging between 5 and 40 microns. The operating condition of 185 kV voltage and 400-µA current was appropriate for the best balance of resolution and energy to enter the specimen. The equipment scanned the entire length of the specimen (approximately 107 mm) in two stacks, which were later stitched together for the complete analysis (Crandall et al. 2018). However, the edge effects and CT scanning artifacts obstructed the scan of the microcracks at both edges of the cylindrical specimen (Cnudde and Boone 2013).

The X-ray CT equipment scanned the entire length of a cylindrical specimen in the form of radiographs, and NSI's Efx-dr software reconstructed the radiographs and produced 2D cross-sectional slices, as shown in Fig. 6a. As the approximate length of shale specimens was 107 mm, and spacing between two consecutive images was 29.9 microns, X-ray CT scan produced 3578 images, approximately for each specimen. In 2D, the pixel resolution of each image was 29.9 microns. In Fig. 6a, the scattered bright area showed the presence of high-density mineral: pyrite (Xradia 2010). The sequential stacking of 2D images reconstructed the 3D image of the scanned specimen, as shown in Fig. 6b. In 3D, the voxel resolution was also 29.9 microns. In Fig. 6b, the superficial cracks and uneven surface of the specimen were visible. The darker region at the core of specimen was an example of the residual beam-hardening artifact in CT-scanned images, discussed in depth in the following section.
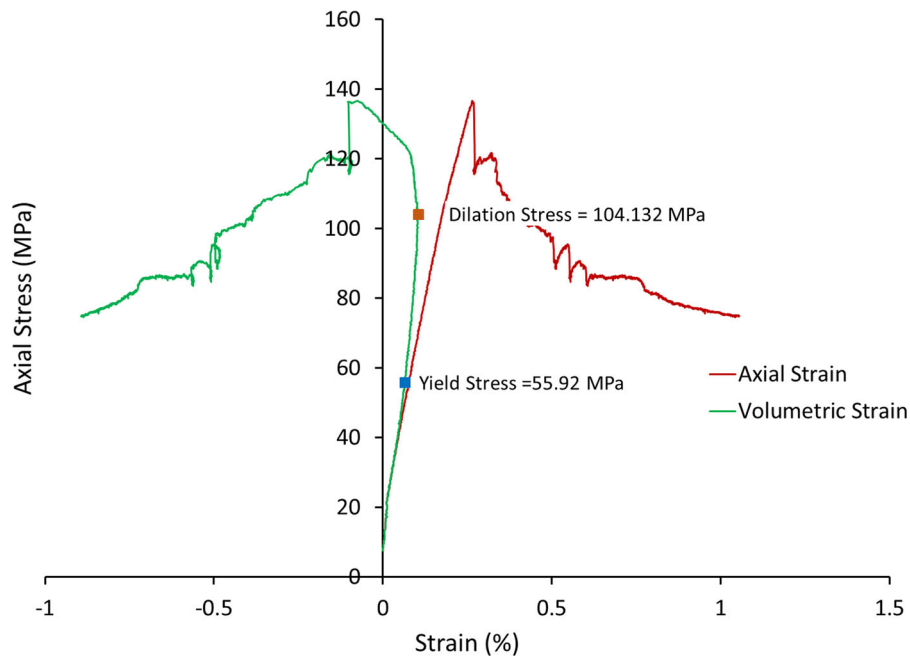
Fig. 5 Axial stress-volumetric strain curve for parallel bedded Marcellus shale at confining pressure of 6.89 MPa
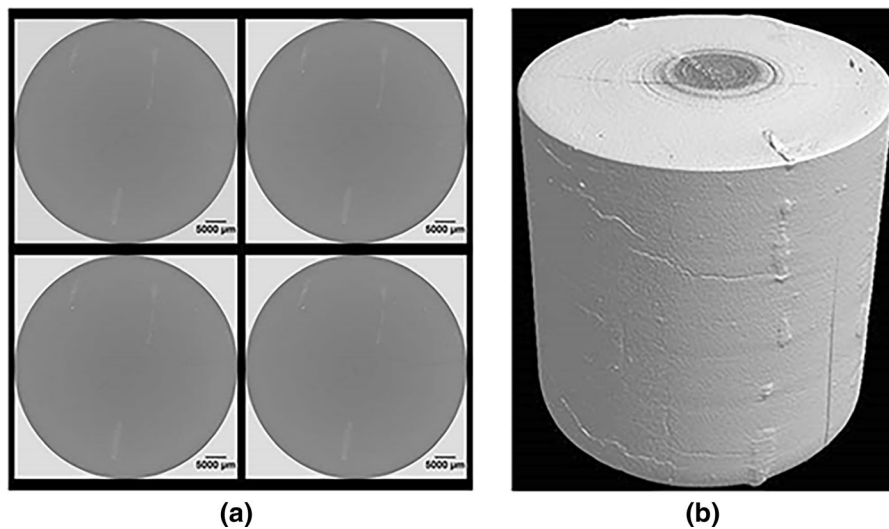

Fig. 6 a 2D X-ray CT images of shale specimen; **b** 3D image reconstructed from the stack of 2D images

The authors also confirmed that the unloading or release of stress did not influence the damage accumulated in the specimens at peak stress level, and subsequently the microcrack geometries in post-triaxial stress state. According to Costin (1983), in cyclic loading, unloading and reloading experiments with AE, the AE activity is substantially high at peak stress level and continue at high rate until unloading occurs. During unloading and reloading, the AE activity remained substantially small until the previous maximum stress is reached. This phenomenon is referred as Kaiser effect, that the rock remembers the previous maximum stress state. The small level of AE activity during unloading peak stress implied negligible effects of stress release on microcracks. Later, the study of fracture process zone in granite specimens

using acoustic emission and optical microscope by Labuz et al. (1987) proposed that an effective crack is composed of traction free length and ligament process zone. They found that, under applied stress, the crack remains fully opened, while upon unloading, the ligament process zone closes back due to interlocking and traction free length remains open. In current research, the image processing techniques only analyzed open cracks, which appeared black in CT images. And, considering the available literature, the authors believed that the release of stress might have closed the interlocked or unbroken ligament zone, while it did not influence the open, traction-free length of microcracks.

2.3 X-Ray CT Image Processing

An image is a definite array of pixels containing digital information of the scanned object. Converting an image into digital form to extract useful information is called image processing (Bernasconi 2005). In the current study, FIJI processed the X-ray CT images through a series of steps, shown in Fig. 7. The methodology of image processing was independent of the location of image along the length of specimen. The method is time-efficient and quite accurate in microcrack segmentation from the rest of the features in the image. It involved the contrast enhancement among different features of the image, automated microcrack segmentation and noise reduction which are discussed in detail in the following subsections.

2.3.1 Contrast Enhancement of Original X-Ray CT Image

The first step of X-ray CT image processing was contrast enhancement of the original X-ray CT image. The constituent minerals of shale, such as calcite, quartz and illite had comparable bulk density (Gupta et al. 2018); therefore, the original X-ray CT image appeared homogenous with no visible microcracks. Although the readjustment of the brightness and contrast of the image showed the microcracks at the microns level resolution, the residual beam-hardening effect restrained the microcrack visualization in the middle region of the specimen.

In the X-ray CT image, an incident X-ray beam attenuates while passing through the material, such that the rate of attenuation depends on the composition and density of the material. However, in the laboratory, the incident polychromatic X-ray beam (a range of the energy spectrum) does not attenuate uniformly while passing through an object. Therefore, even in a homogenous object, the 2D image contains brighter pixels at the edge and darker pixels in the middle regions. The artifact is called beam-hardening artifact, implies false information about the specimen composition and density. Although the X-ray CT image reconstruction software pre-corrects the artifact, the residual beam-hardening artifact restricts the applicability of conventional brightness and contrast adjustment.

In the X-ray CT image, the intensity of residual beam hardening artifact is determined through the variation in the profile of gray scale value (GSV)
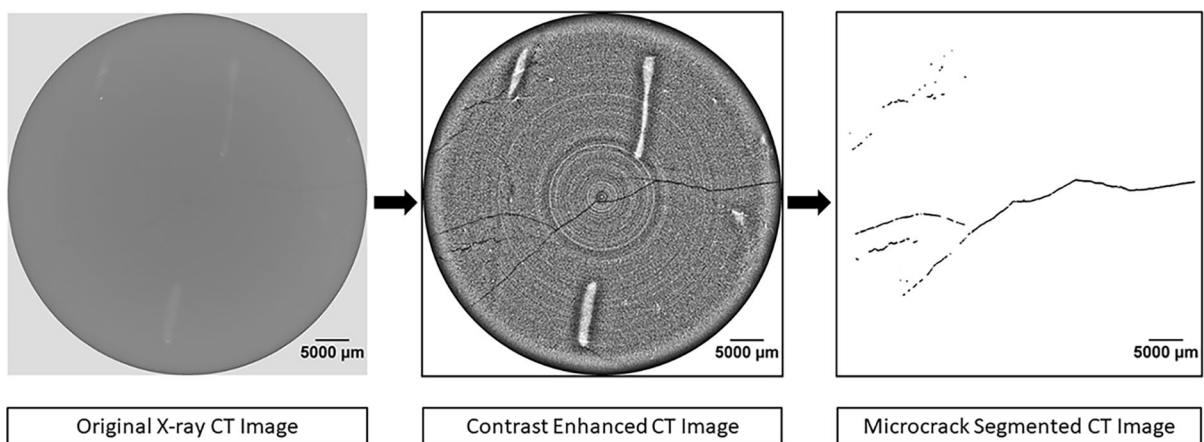

Fig. 7 Methodology of X-ray CT image processing

across the width of image. For example, Fig. 8 showed the comparison of GSV of the image along the specimen diameter at three different contrast levels. Figure 8a was the original CT image; Fig. 8b was the similar CT image with a manual readjustment of brightness and contrast; and Fig. 8c was the similar image with locally enhanced contrast. In Fig. 8, the profile of GSV showed that both (a) and (b) had a cupping artifact, such that the shape of a cup was visible in the middle region of the profile. The beam-hardening effect is also called a cupping artifact, indicating the presence of comparatively darker pixels in the region. Although the residual beam-hardening artifact is small in the original X-ray CT image, the manual readjustment of brightness and contrast enhanced the artifact (Mohapatra 2012). Therefore, a plugin called local contrast enhancement (CLAHE) in FIJI was used to improve the image contrast (Zuiderveld 1994). As shown in the GSV plot of Fig. 8c, although the GSV was continuously changing between consecutive points, the cupping artifact was absent. The image also showed microcracks in the whole region up to the image resolution. The appropriate parameter values in the plugin were determined through iterations.

2.3.2 Crack Area Segmentation

The next step of image processing was the segmentation of the microcrack from the contrast-enhanced X-ray CT image, as shown in Fig. 6. Although global thresholding is a conventional technique of segmenting different features in an image (Promentilla et al. 2009), the method does not always yield good results. The common reasons are low contrast among different features in the image, beam-hardening artifact (Waarsing et al. 2004). There are many different, time-efficient algorithms used for desired feature segmentation (Waarsing et al. 2004; Voorn et al. 2013; Wang et al. 2013). In the current study, a plugin named trainable weka segmentation (TWS) in FIJI efficiently segmented microcracks from intact rock (Arena et al. 2014). The plugin runs on a machine-learning algorithm with a set of particular image features to provide pixel-based segmentation (Arganda-Carreras 2017).

2.3.3 Noise Reduction

Although the TWS plugin produced directly useable microcrack mages, the last step of image processing was noise reduction from the microcrack-segmented X-ray CT image. Sometimes the images segmented
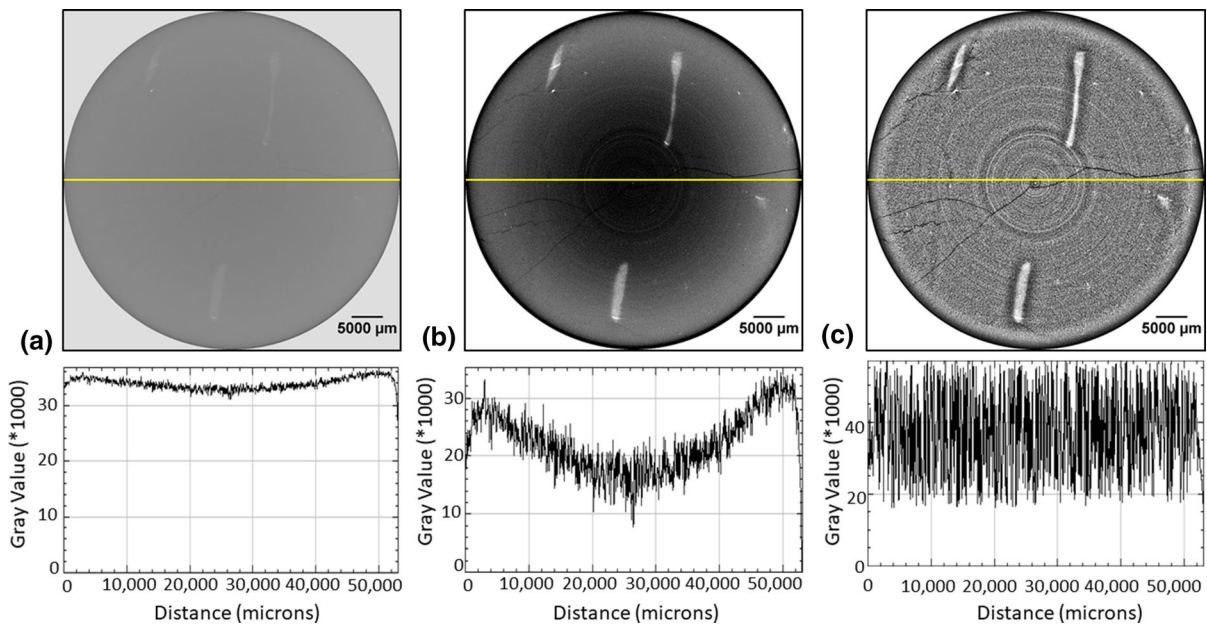

Fig. 8 Comparison of GSV along the yellow line among similar X-ray CT images at different contrast levels: **a** original X-ray CT image; **b** conventional brightness and contrast adjusted X-ray CT image; **c** local contrast enhanced X-ray CT image

through automated process possessed sparsely occurring black and white pixels, also called salt-and-pepper noise (Guo et al. 2014). Tool like "Remove Outliers" eliminated the extraneous black pixels scattered in the image (Ferreira and Rasband 2012). The tool is a median filter that replaced each pixel with a median value in its 3 * 3 neighborhood. The process of noise reduction was based on the manual comparison of crack segmented images with the contrast enhanced CT images.

These three steps of image processing produced noise-free microcrack-segmented 2D images. For the purpose of consistency, the values of the parameters in plugin CLAHE and TWS remained same throughout the image processing of different specimens. Based on the type of rock specimen, the value of the parameters in plugin CLAHE and TWS might change, however, the process is equally applicable on other types of sedimentary rocks.

3 Results and Discussions

3.1 Mechanical Deformation of Bedded Shale Specimens

The average differential strength of Marcellus shale at 6.89 MPa confining pressure was 135.84 MPa, and 125.26 MPa with beds parallel and perpendicular to the direction of major principal stress, respectively. Based on the differential strength, three specimens of both types of bedding orientation were subjected to three successive levels of differential stress. The results of the triaxial tests, such as the value of axial stress, accumulated permanent strain in the specimen, modulus of elasticity and Poisson's ratio were summarized in Table 3. In this analysis, the ASTM recommended secant method was used to determine the modulus of elasticity (ASTM 2014), such that secant modulus was determined from zero stress to the stress equivalent to the 40% of the fracture strength. The permanent strain was unrecovered strain in the specimen at zero differential stress (Mogi 2006). Based on the correlation among AE activity and axial stress–strain curve, shown in Fig. 2, we also analyzed the axial stress and volumetric strain curve of each specimen and identified the different stages of microcrack development. The axial stress-volumetric strain curve for each specimen in loading and unloading

condition was shown in Fig. 9. Based on the permanent deformation in the specimen and nature of axial stress-volumetric strain curve, the important observations were:

1. The modulus of elasticity and Poisson's ratio was different among similarly bedded shale specimens at equal confining stress, as shown in Table 3. In addition, the modulus of elasticity was comparatively higher for perpendicular bedded specimens than the parallel bedded specimens.

2. The axial stress-volumetric strain curve of specimen PD-35 showed non-linear elastic behavior (Jaeger and Cook 1976). The stress–strain curve was similar in loading and unloading condition and permanent deformation was significantly small, indicating towards small specimen consolidation. It implied that the differential stress equivalent to 55% of differential strength was in the elastic limit of perpendicular bedded specimen. In Fig. 2, the comparison of axial stress against volumetric strain indicated the specimen to be in the elastic range.

3. For specimen PD-36, the differential stress equivalent to 65% of the differential strength caused permanent volumetric deformation of − 0.0085%. According to Alejano and Alonso (2005), between the initiation of stable fracture propagation and the onset of unstable facture propagation, permanent strain in radial direction is a negative value, whereas permanent strain in axial strain is null.

4. For specimen PD-30, the permanent volumetric deformation was 0.034% at the differential stress equivalent to 70% of the differential strength. In Fig. 2, the comparison of axial stress-volumetric strain curve indicated that specimen PD-30 was in the region of stable crack growth before reaching to the point of crack coalescence. The axial stress-volumetric strain in unloading condition was not captured due to the error in the data acquisition system. At the end of the unloading, the readings of axial and lateral LVDT was manually recorded as permanent strain in axial and radial direction.

5. For specimen PL-32, the permanent volumetric deformation was 0.0167% at differential stress equivalent to 55% of the differential strength. In Fig. 2, the axial stress-volumetric strain curve in loading condition indicated the specimen in the

Table 3 Results of triaxial compression tests on bedded shale specimens

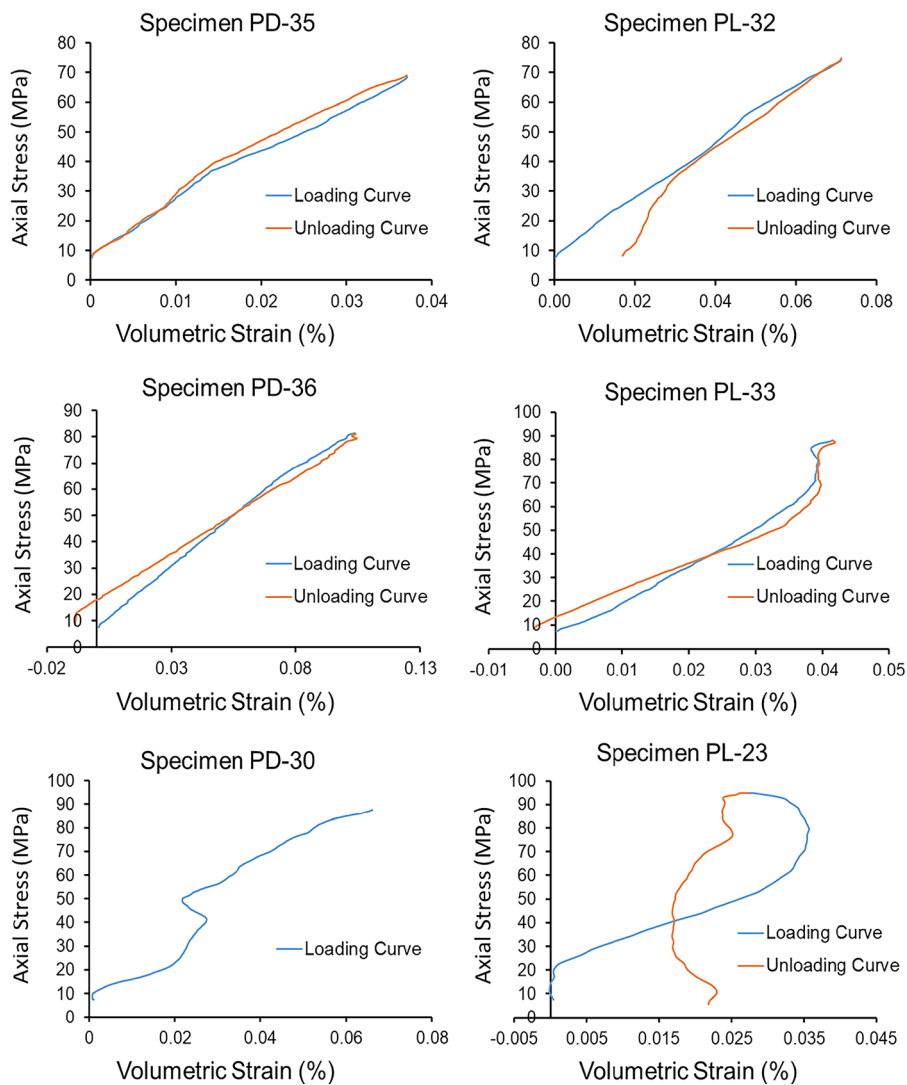| Specimen ID	Specimen type	Triaxial stress state		Level of differential stress (% of differential strength)	Permanent strain (%)			Secant modulus of elasticity (GPa)	Poisson's ratio
		Confining stress (MPa)	Axial stress (MPa)		Axial strain	Radial strain	Volumetric strain		
PD-35	Perpendicular	6.89	68.89	55	0.0005	− 0.0001	0.0003	186.48	0.04
PD-36		6.89	81.31	65	0.0001	− 0.0043	− 0.0085	70.17	0.06
PD-30		6.89	87.68	70	0.0414	− 0.004	0.034	149.12	0.19
PL-32	Parallel	6.89	74.63	55	0.017	− 0.0001	0.0167	93.04	0.05
PL-33		6.89	88.15	65	0.001	− 0.0022	− 0.0032	69.13	0.28
PL-23		6.89	94.98	70	0.023	0.00	0.023	99.12	0.04

Fig. 9 Axial stress-volumetric strain curve under triaxial stress state

region of crack closure and elastic deformation. Although the specimen recovered 0.0536% volumetric strain upon unloading, significant permanent volumetric strain of 0.0167% accumulated in the specimen, indicating towards significant specimen consolidation.

6   For specimen PL-33, the permanent volumetric deformation was $-$ 0.0032% at differential stress equivalent to 65% of the differential strength. Similar to perpendicular bedded specimen PD-36, specimen PL-33 lied between the initiation of stable crack propagation and the onset of unstable fracture propagation.

7   For specimen PL-23, the permanent volumetric deformation was 0.023% at differential stress equivalent to 70% of the differential strength. The axial stress against volumetric strain curve showed that the specimen reached to the maximum positive volumetric strain condition and entered the state of dilation. According to Fig. 2, specimen PL-23 had entered the region of coalescnece of microcracks.

3.2 Geometry of Microcracks from X-Ray CT Image Processing

The mechanical behavior of rocks strongly depends on the morphology of microcracks and pore space (Mavko and Nur 1978). According to Simmons and Richter (1976), for 2D microcracks, one dimension is much smaller than the other, such that the ratio of width and length, also called as aspect ratio is less than 10^{-2}, and typically in the range of 10^{-3} and 10^{-5}. Analytically, the closed form solutions only exist for elliptical or ellipsoidal crack shapes, and, consequently, the shape of the cracks is assumed as 2D elliptical or 3D ellipsoidal (O'Connell and Budiansky 1974; Budiansky and O'Connell 1976). However, direct visual inspection suggested that microcracks in rocks are irregular in shape with a wide range of edge configurations (Mavko and Nur 1978). The discrepancy in the shape of microcracks affects the compliance nature of cracks over a range of pressures, leading to a different stress–strain behavior of the rock.

In the X-ray CT image, minerals with high density, thickness block a larger portion of incident X-ray energy than minerals with lower density (Xradia

2010). Therefore, the low-density areas, such as microcracks appears dark, while high-density areas, such as intact rock appears bright (Rodriguez et al. 2014). As shown in Fig. 10a, in current study, observed microcracks were thin linear, black-colored features with random orientation and irregular shape. While, the intact rock was gray with high density pyrite mineral in the top-right corner. Further, based on the aspect ratio, the 2D microcracks were identified in X-ray CT image. In 3D, the sequential stacking of 2D microcracks generated a rectangular plate-like structure with the length and width much higher than the aperture, as shown in Fig. 10b. The results of geometry of microcracks in two- and three-dimensions were described in following sections.

3.2.1 2D Geometry of Microcracks

The 2D geometry of microcracks included area, aperture, and length of microcracks in 2D coordinate system. As the visualization of microcracks depends on the resolution of imaging technique, sometimes individual microcracks cannot be distinguished from long array of small microcracks (Kranz 1983). Therefore, the parameter like number of microcracks was not included in this analysis. In addition to the image processing, different plugins in FIJI determined the different 2D geometrical parameters of microcracks, briefly explained by Gupta (2019). As the X-ray CT image processing determined 2D geometrical parameters for an individual image, the authors used average value of respective parameters to characterize the 2D microcrack geometry for an entire specimen. For example, average area represented the ratio of sum of area of microcracks of each image and total number of 2D images (n) (Eq. 2). Similarly, the average aperture was ratio of sum of aperture of microcracks in each image and total number of 2D images. The average values of 2D geometrical parameters of microcracks in pre- and post-triaxial stress state were summarized in Table 4. As the specimen was scanned in pre-and post-triaxial test state, the comparison between the respective parameters also determined the stress-induced changes in the 2D geometry of microcracks (Eq. 3).

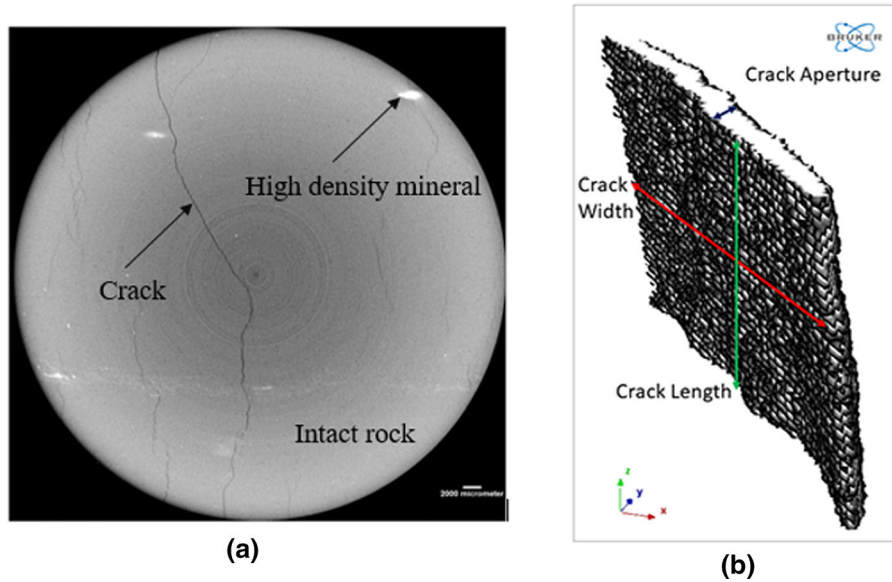$$Average\ area = \frac{\sum_{i=1}^{n} area_i}{n}$$

Fig. 10 **a** 2D X-ray CT image with crack and intact rock; **b** 3D structure of microcrack

$$Average\ aperture = \frac{\sum_{i=1}^{n} aperture_i}{n}$$

$$Average\ length = \frac{\sum_{i=1}^{n} length_i}{n} \qquad (2)$$

$$Stress\ induced\ change\ in\ Average\ area\ (\%)$$
$$= \frac{\left(Average\ area_{post\ triaxial} - Average\ area_{pre\ triaxial}\right)}{\left(Average\ area_{pre\ triaxial}\right)}$$
$$* 100$$
$$(3)$$

In Table 4, the small value of average aspect ratio ($1.4 * 10^{-3}$–$2.1 * 10^{-2}$) confirmed that the analyzed features were microcracks in shale specimens. The results of microcrack geometry in pre-triaxial stress state showed that each specimen contained significant density of microcracks, called as pre-existing microcracks (Kranz 1983). According to Nur and Simmons (1970), pre-existing microcracks are formed either due to natural processes including pressure or temperature over geological time, or mechanically due to changes in stresses during coring process. However, the stress-induced changes in the area of microcracks showed that differential stress primarily reduced the area of pre-existing microcracks in specimen PD-35, PD-36, PL-32 and PL-33. While, in specimen PD-30 and PL-23, the differential stress increased the average area of microcracks. It implied that the differential stress

equivalent to 55% and 65% of differential strength caused closure of pre-existing microcracks in both parallel and perpendicular bedded shale specimen. However, the differential stress equivalent to 70% of the differential strength caused either increase in the area of pre-existing microcracks, or nucleated new microcracks in both parallel and perpendicular bedded shale specimen.

The geometrical reason for change in the average area of pre-existing microcracks was analyzed through the comparison of change in average value of aperture and length of microcracks with the average area of microcracks, as shown in Fig. 11. The comparisons implied that the differential stress equivalent to 55% and 65% of differential strength significantly reduced both aperture, and length of microcracks in specimen PD-35, PD-36, PL-32, and PL-33. However, differential stress equivalent to 70% of the differential strength increased the length of microcracks in perpendicular bedded specimen, PD-30, and aperture of microcracks in parallel bedded specimen, PL-23.

3.2.2 3D Geometry of Microcracks

The 3D geometry of microcracks included volume, weighted-mean aperture, and area of plane of microcracks in 3D coordinate system. Similar to the 2D analysis, different plugins in FIJI determined

Table 4 2D geometrical parameters of microcracks in pre- and post-triaxial stress state

| Specimen ID	Axial stress (MPa)	Pre-triaxial stress				Post-triaxial stress				Stress-induced change (%)		
		Average area (mm^2)	Average aperture (mm)	Average length (mm)	Average aspect ratio	Average area (mm^2)	Average aperture (mm)	Average length (mm)	Average aspect ratio	Average area	Average aperture	Average length
PD-35	68.89	2.23	0.075	14.99	$5.0 * 10^{-3}$	1.65	0.063	12.14	$5.2 * 10^{-3}$	− 26.28	− 15.67	− 19.01
PD-36	81.31	3.16	0.074	22.31	$3.3 * 10^{-3}$	2.36	0.058	18.21	$3.2 * 10^{-3}$	− 25.48	− 21.19	− 18.38
PD-30	87.68	7.08	0.114	52.05	$2.2 * 10^{-3}$	11.21	0.109	78.76	$1.4 * 10^{-3}$	58.29	− 3.44	51.31
PL-32	74.63	1.81	0.084	11.05	$7.6 * 10^{-3}$	0.38	0.057	2.75	$2.1 * 10^{-2}$	− 78.98	− 31.26	− 75.11
PL-33	88.15	2.03	0.101	12.38	$8.2 * 10^{-3}$	1.17	0.071	9.61	$7.4 * 10^{-3}$	− 42.34	− 29.93	− 22.37
PL-23	94.98	8.62	0.107	68.04	$1.6 * 10^{-3}$	9.7	0.119	63.45	$1.9 * 10^{-3}$	12.54	12.14	− 6.75
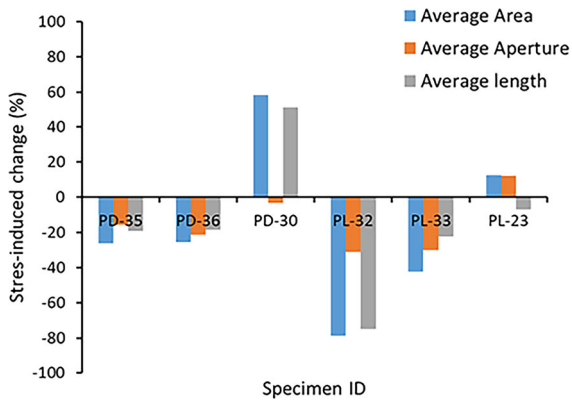
Fig. 11 Comparison of the stress-induced change in the average value of area, aperture, and length of microcracks in each specimen

individual 3D geometrical parameter of microcracks (Gupta 2019). In 3D, the area of plane of microcracks did not represent the surface area of microcrack; rather it represented the area of plane of microcrack perpendicular to the direction of 3D aperture. For example, in Fig. 10b, the 3D aperrure of microcrack was parallel to the y-direction. And, the area of plane of microcrack belonged to the x–z plane, perpendicular to the y-direction.

The results of the 3D geometry of microcracks, like total volume, weighted-mean aperture and area of plane of microcracks, and stress-induced change in respective parameters (Eq. 4) were summarized in Table 5. Similar to the 2D geometry, the 3D geometry of microcracks in pre-triaxial stress state indicated the significant presence of pre-existing microcracks. The stress-induced percentage change in total volume of

microcracks showed that the differential stress equivalent to 55% and 65% of differential strength caused partial closure of pre-existing microcracks, and decreased the microcrack volume in specimen PD-35, PD-36, PL-32, and PL-33. However, differential stress equivalent to 70% of differential strength either enhanced the volume of pre-existing microcracks or nucleated new microcracks in specimen PD-30 and PL-23.

$$Stress\ induced\ change\ in\ Total\ Volume\,(\%)$$
$$= \frac{\left(Total\ Volume_{post\ triaxial} - Total\ Volume_{pre\ triaxial}\right)}{\left(Total\ Volume_{pre\ triaxial}\right)}$$
$$* 100$$

(4)

The geometrical reason of change in total volume of microcracks was analyzed through the comparison of stress-induced change in weighted-mean aperture and area of plane of microcracks with total volume of microcracks, as shown in Fig. 12. The comparisons showed that percentage change in both weighted-mean aperture and area of microcracks was significant in specimens PD-35, PD-36, PL-32, and PL-33. However, specimens like PD-30 and PL-23 had different behavior. For example, specimen PD-30 experienced significant changes in the area of plane of microcracks, while the weighted-mean aperture remained approximately same. However, specimen PL-23 experienced significant changes in the weighted-mean aperture of microcracks only. It was concluded that the differential stress equivalent to 55% and 65% of differential strength contracted total crack volume through the contraction of both area of

Table 5 3D geometrical parameters of microcracks in pre- and post-triaxial stress state

| Specimen ID	Axial stress (MPa)	Pre-Triaxial Stress			Post-Triaxial Stress			Stress-induced change (%)		
		Total volume (mm^3)	Weighted-mean aperture (mm)	Area of plane (mm^2)	Total volume (mm^3)	Weighted-mean aperture (mm)	Area of plane (mm^2)	Total volume	Mean 3D aperture	Total area
PD-35	68.89	231.71	0.126	1653.77	166.04	0.123	1306.04	− 28.34	− 3.12	− 20.16
PD-36	81.31	330.04	0.133	2434.9	240.46	0.122	1968.4	− 27.14	− 7.91	− 19.16
PD-30	87.68	771.50	0.136	5859.09	1186.94	0.135	9046.73	53.85	− 0.95	54.4
PL-32	74.63	185.24	0.091	1205.1	36.58	0.086	296.9	− 80.25	− 6.29	− 75.36
PL-33	88.15	208.95	0.125	1335.9	117.85	0.107	1048.8	− 43.59	− 14.18	− 21.49
PL-23	94.98	936.22	0.138	7619.83	1063.29	0.160	7487.84	13.57	16.24	− 1.73
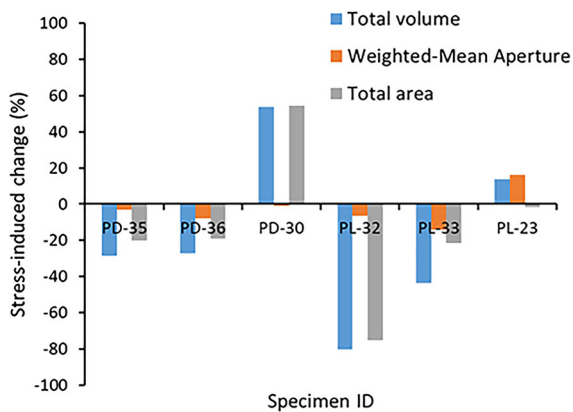
Fig. 12 The comparison of stress-induced change in total volume of microcracks with weighted-mean aperture and area of plane of microcracks

plane and aperture. While, the differential stress equivalent to 70% of differential strength increased the total crack volume through increase in total area of microcracks in specimen PD-30, and weighted-mean aperture in specimen PL-23. In addition, the authors also confirmed the 3D rectangular plate geometry of microcracks. For a 3D rectangular cuboid, total volume is equivalent to the product of each of three dimensions. As authors presumed that the area of plane of microcracks represents the product of the crack length and crack width, the total volume of microcracks was calculated as the product of the weighted-mean aperture and area of plane of microcracks. The calculated volume of microcracks was compared with measured volume of microcracks in Table 5. Figure 13 showed the statistical comparison between two types of crack volume. The significantly
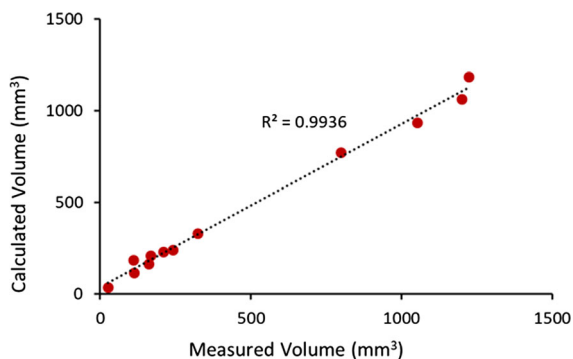

Fig. 13 Statistical comparison between calculated and measured volume of microcracks for shale specimens

high value of coefficient of correlation (R^2) of 0.99 indicated that the 3D microcracks should be best approximated as 3D rectangular plate.

The 3D surface of microcracks was also generated in Bruker Computed Tomography Analyzer (CTAn) software, such that local 3D aperture of microcracks were classified into three intervals, represented by three colors in Figs. 14 and 15. Red represented the local 3D aperture between 0.029 and 0.087 mm, green represented the local 3D aperture between 0.087 and 0.203 mm, and blue represented the local 3D aperture between 0.203 and 0.319 mm. The comparison of 3D surface of microcracks in pre-and post-triaxial stress state showed that pre-existing, naturally occurring microcracks contracted under differential stress in specimen PD-35, PD-36, PL-32, and PL-33. However, specimen PD-30 contained a new stress-induced plane of microcracks and comparatively lesser density of green and blue colored microcracks in post-triaxial stress state. It explained the significantly high percentage change in total area of microcracks and decrease in weighted-mean 3D aperture in specimen PD-30. While, in specimen PL-23, the pre-existing plane of microcracks appeared dense with high density of green colored microcracks in post-triaxial stress state. The increase in green color microcracks in specimen PL-23 explained the high percentage increase in the 3D weighted-mean aperture of microcracks.

Based on the comparison of 2D and 3D geometry of microcracks in pre-and post-triaxial stress state, the authors found that differential stress equivalent to 55% and 65% of differential strength contracted the pre-existing microcracks, and the orientation of bedding plane had negligible influence. However, differential stress equivalent to 70% of differential strength propagated the pre-existing microcracks and nucleated new microcracks in the specimen. In addition, orientation of bedding plane influenced the nature of propagation of microcracks.

3.2.3 Visual Representation of the Stress-Induced Change in the Geometry of Microcracks

FIJI determined the area of microcracks for each 2D image of a specimen in pre- and post-triaxial stress state. The graph between 2D area of microcracks of each image and individual image position analyzed the distribution of area of microcracks along the length of
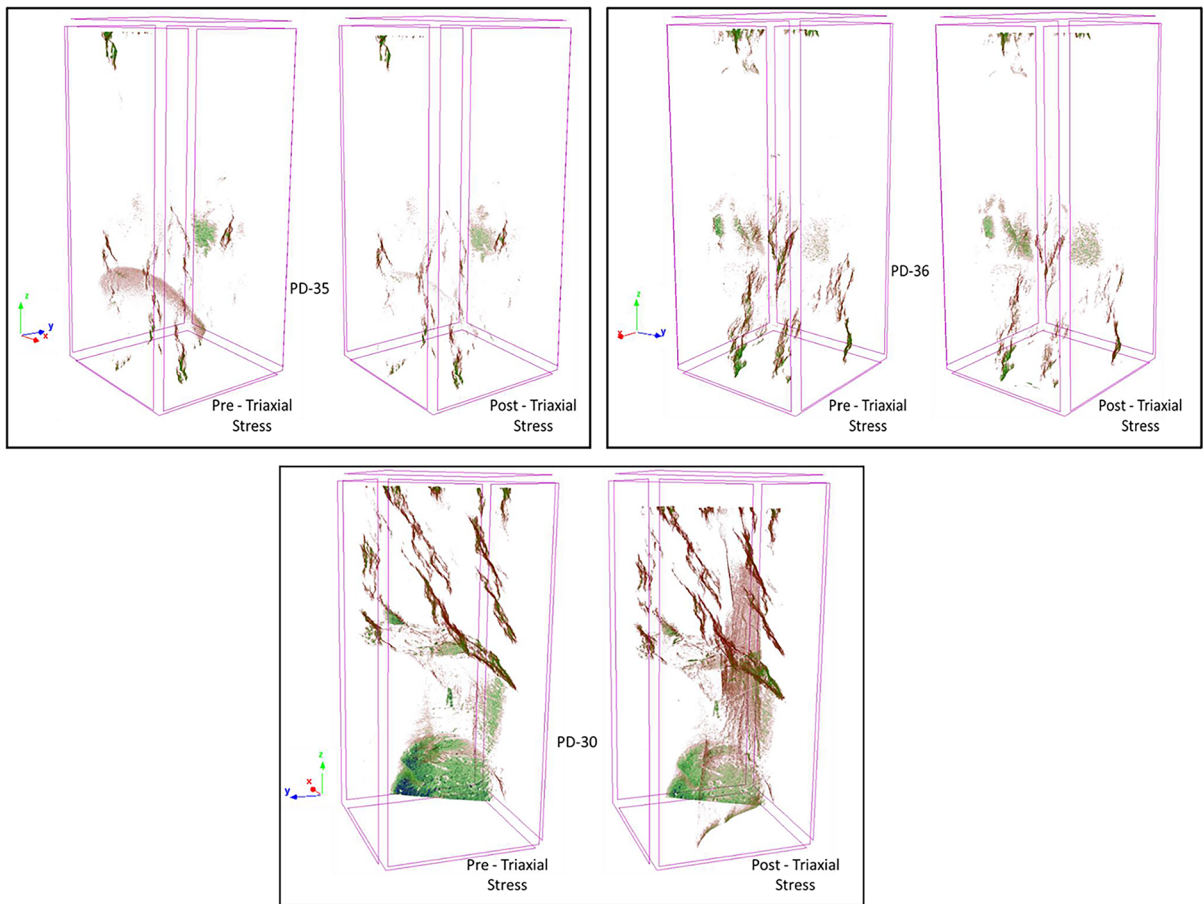
Fig. 14 3D distribution of microcracks in pre-and post- triaxial stress state in perpendicular bedded specimens

the specimen. As shown in Fig. 16, the graph was drawn for each specimen in pre-and post-triaxial stress state. In Fig. 16, the reason of zero crack area at either end was the limitation of X-ray CT equipment in visualizing cracks at the specimen edge. The Fig. 16 showed that, although the value of cumulative area of microcrack was different in pre- and post-triaxial stress state, the nature of the distribution of area of microcracks was similar in pre-and post-triaxial stress state. The area of microcracks was either equal or lower in post-triaxial stress state compared to pre-triaxial stress state for specimens like PD-35, PL-32, PD-36, and PL-33. However, specimens like PD-30 and PL-23 had either higher or equal value of cumulative area of microcracks in post-triaxial stress state compared to the pre-triaxial stress state. The decrease in the 2D area of microcracks in specimens PD-35, PD-36, PL-32, and PL-33 indicated the partial closure of pre-existing microcracks due to applied

triaxial stresses (Brantut 2015). However, in specimens PD-30 and PL-23, the 2D area of microcracks increased due to stresses. The possible reason was nucleation of new microcracks, increase in the length or aperture of pre-existing microcracks (Griffiths et al. 2017).

Another method for the comparison of 2D microcracks in pre- and post-triaxial stress state was vertical projection of microcracks on a 2D plane, as shown in Fig. 17. The figure also showed that differential stress equivalent to 55% and 65% of differential strength significantly reduced the density of pre-existing microcracks in specimen PD-35, PD-36, PL-32, and PL-33. However, it also showed that, at few places marked by red boundary in post-triaxial stress state, few new microcracks also nucleated in specimen PD-35, PD-36, and PL-33. In specimen PD-36, few pre-existing microcracks also propagated, enclosed in the green colored boundary in Fig. 16. In addition, the
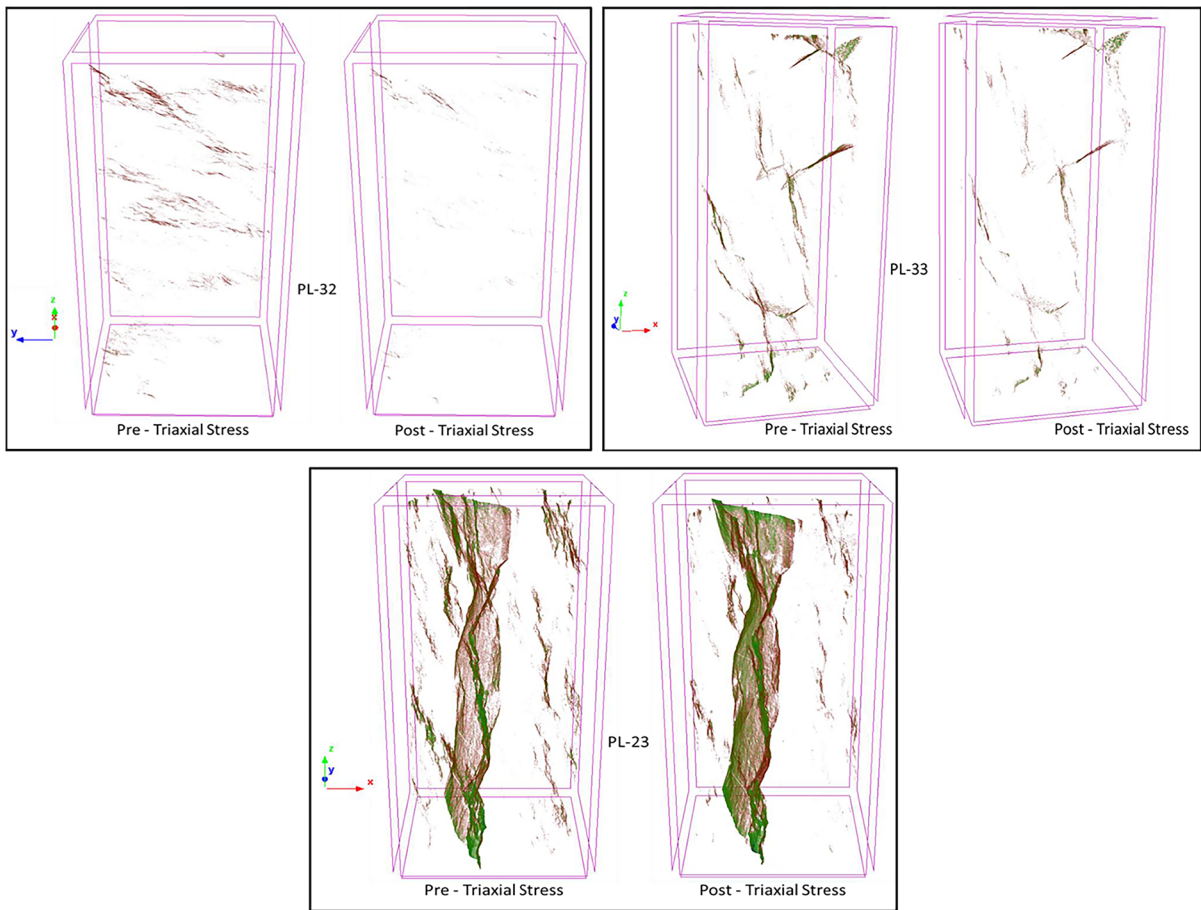
Fig. 15 3D distribution of microcracks in pre-and post- triaxial stress state in parallel bedded specimens

differential stress equivalent to 70% of differential strength induced a new plane of microcracks in specimen PD-30 and PL-23, enclosed in the red colored boundary sketch in Fig. 17. The high differential stress also filled the vacant portion in pre-existing plane of microcracks in specimen PL-23.

In addition to these methods, the individual 2D microcrack images in pre-and post-triaxial stress state were compared to see the nature of change in the geometry of microcracks. For example, in Fig. 16, the data points marked red for specimen PD-35, and purple for specimen PD-30 represented the similar individual image in pre-and post-triaxial stress state. As the triaxial stress consolidated the specimen, the length of the specimen reduced and the graph of area of microcracks and individual image position in post-triaxial stress state lied to the left of pre-triaxial stress state. Figure 18 showed the comparison of image of

microcrack (red data point) in pre-and post-triaxial stress state for specimen PD-35. The applied stress significantly contracted the entire surface of the microcrack number 1 enclosed in the solid red boundary and caused multiple selective discontinuities in the microcrack surface number 2, enclosed in dashed red boundary. The contraction of the entire crack surface occurred in the complete specimen, and caused 26.28% contraction in the 2D average area of pre-existing microcracks (refer to Table 4). Similar to the multiple contraction of microcrack number 2 in Fig. 18, Batzle et al. (1980) and Liu et al. (2001) reported on the transformation of one single crack into several smaller cracks, with significantly shorter lengths with similar crack aperture under stress conditions. According to Kranz (1983), the closure rate of microcracks depends on the asperity. Factors, such as shape and roughness of the cracks, the relative
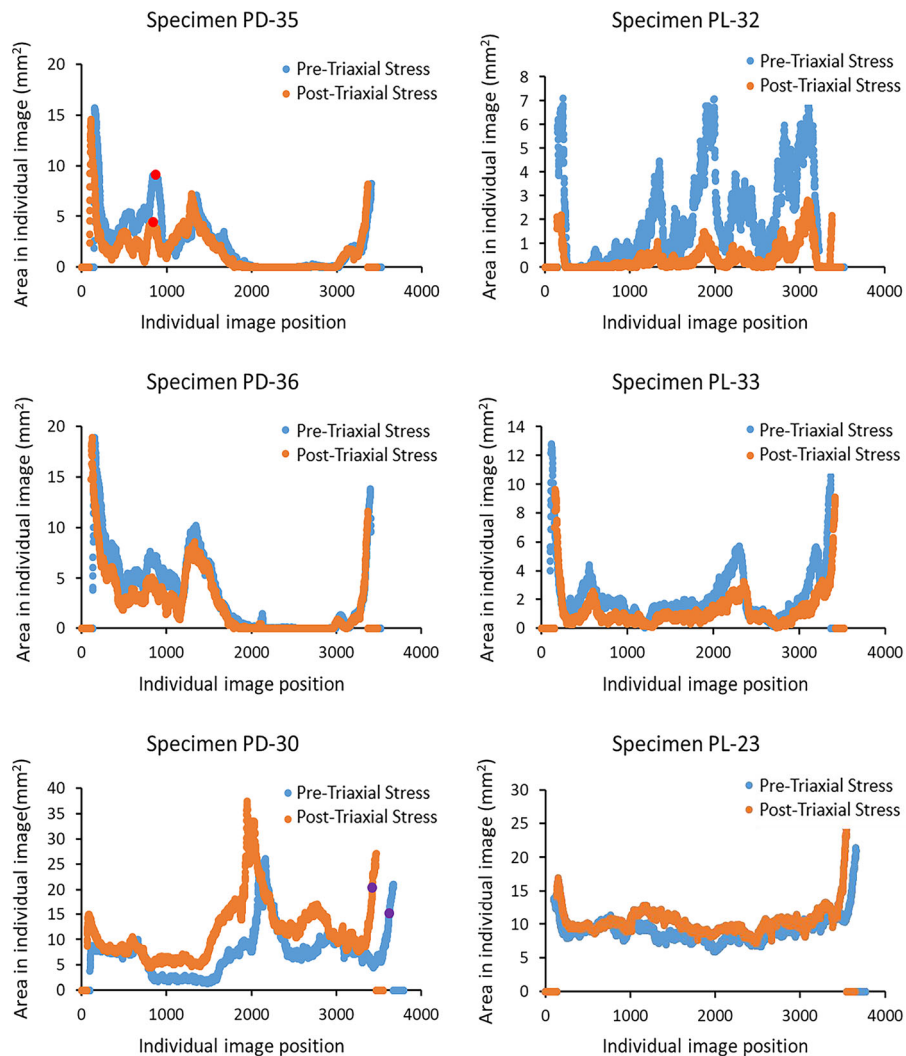
Fig. 16 The graph between the area of microcracks in individual image and individual image position

position of crack walls, and crack orientation with respect to applied stress affect the non-uniform contraction of microcracks (Wu et al. 2014). Almisned et al. (2017) also found that initially increasing the axial load in triaxial stress state causes closure of pre-existing microcracks in homogenous and laminated sandstone.

Another visual comparison of microcracks in pre- and post-triaxial stress state was shown in Fig. 19 for specimen PD-30. Here, the stress-induced change in the geometry of microcracks was compared at three locations. The applied stress induced a new microcrack at location 1 and extended microcrack through rock bridges at location 2. However, at location 3 pre-

existing, microcrack discontinued into two microcracks. The propagation of a crack through the rock bridge and the formation of a new microcrack showed the predominant influence of an increase in crack length on the change of the crack area. It also showed that, even at high differential stress, few pre-existing microcracks were closed.

The extension of pre-existing cracks along the length was due to the presence of the fracture process zone (FPZ) at the crack tip (Labuz et al. 1987). The triaxial stress on the pre-existing microcracks in brittle shale caused the formation of the process zone at the microcrack tip due to reduced hardness and modulus in the cracked region compared to intact rock. Brooks
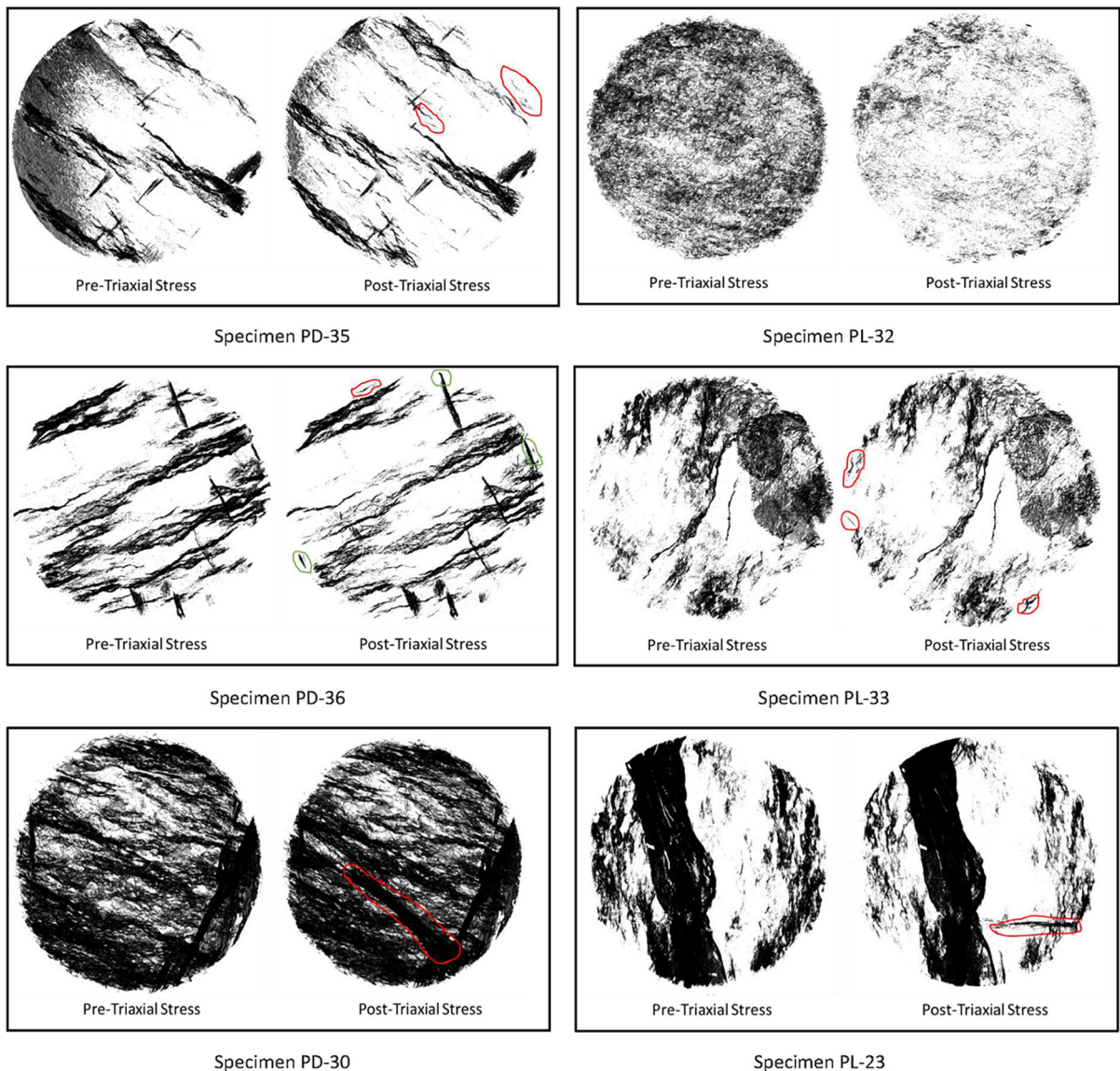
Fig. 17 Comparison of vertical projection of 2D microcracks in shale specimen

(2010) and Bobko (2008) found that, in marble and shale, FPZ possessed reduced nanoindentation hardness and nanoindentation modulus. Cui and Han (2018) showed the in situ growth of an artificially incised notch in brittle shale under tensile apparatus through a scanning electron microscope. They observed that continuous generation and coalescence of the damage zone, which existed around the crack tip when tensile stresses are concentrated, caused the advancement of microcrack.

3.3 Comparison of Permanent Deformation and Stress-Induced Change in Geometry of Microcracks

The results of stress-induced changes in the geometry of microcracks, the permanent volumetric strain and the graph between axial stress and volumetric strain analyzed the correlation between macroscopic and microscopic deformation in each specimen. The observations were:
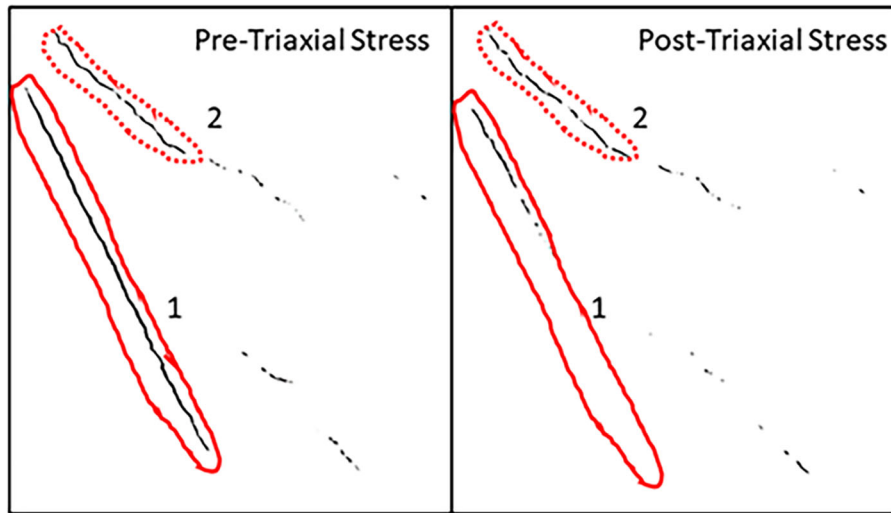
Fig. 18 Visual comparison of 2D geometry of microcracks in specimen PD-35
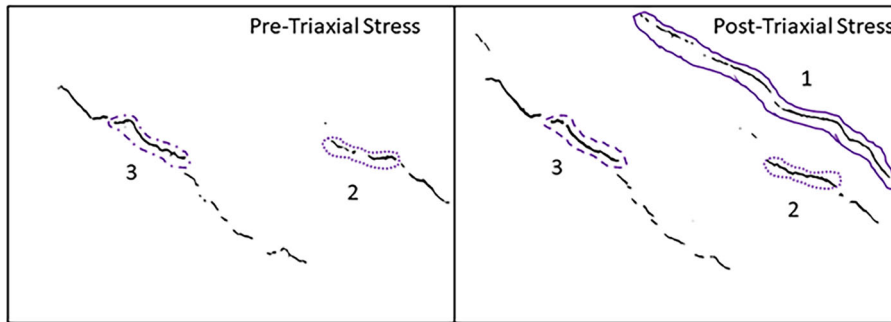

Fig. 19 Visual comparison of 2D geometry of microcracks in specimen PD-30

1. According to Costin (1983) in conventional triaxial tests, the confining pressure closes the pre-existing microcracks, decreases the initial non-linearity of stress–strain curve and increases the stiffness of the rock. In current study, although each specimen was confined with similar pressure of 6.89 MPa, the magnitude of secant modulus of stiffness was considerably different. We concluded that the significant difference in the total volume of microcracks before triaxial tests (referred to Table 4) and the dependence of closure of microcracks on the crack asperity were primary reasons of dissimilarity between secant modulus of stiffness (Kranz 1983; Wu et al. 2014).

2. The graph between axial stress and volumetric strain, and permanent volumetric deformation of specimen PD-35 and PL-32 suggested that the differential stress equivalent to 55% of differential

strength lied in the range of crack closure and elastic limit. However, the differential stress equivalent to 65% of differential strength lied in the range of initiation of stable cracks and onset of unstable crack propagation in bedded specimens PD-36 and PL-33. The comparison of the area, and volume of microcracks in pre- and post-triaxial stress state for respective specimens showed that applied differential stress primarily caused the closure of pre-existing microcracks, reduced both mean 3D aperture and area of plane of microcracks. While the vertical projection of 2D microcracks in specimen PD-35, PD-36, and PL-33 showed the nucleation of few new microcracks too. The nucleation of few microcracks at low stress level might be due to the local yielding of rock specimens through non-uniform distribution of stress (Mogi 2006). The orientation of bedding

plane had no effect on the mode of closure of microcracks. It suggested that the small level of differential stress significantly closes pre-existing microcracks and nucleates few new microcracks.

3 The graph between axial stress and volumetric strain, and permanent volumetric deformation of specimen PD-30 and PL-23 suggested that the differential stress equivalent to 70% of differential strength was in the region of stable crack propagation and crack coalescence in bedded shale specimens. The comparison of the volume of microcracks in pre- and post-triaxial stress states showed that the applied differential stress increased the total volume of microcracks. Therefore, the results from triaxial tests and X-ray CT scan were similar. However, the mode of increase in the volume of microcracks was different in both specimens. The differential stress developed a new, axially oriented plane of microcracks in perpendicular bedded specimen, PD-30 and significantly increased the area of plane of microcracks. However, in PL-23, the applied differential stress significantly increased the mean 3D aperture of microcracks. The possible reason for the difference in the mode of increase in crack volume was orientation of the bedding plane.

3.4 Conclusions

1 The shale specimens had a homogenous composition. However, the elastic parameters were different for similarly bedded specimens at similar axial loading rates and confining stress. A possible reason of specimen heterogeneity was the significant presence of pre-existing microcracks and varying degree of microcrack asperity.

2 The stress-induced changes in the microcrack geometry was influenced by the level of stress and the orientation of the bedding plane. The level of differential stress controlled the nature of change in microcrack geometry, while bedding plane orientation controlled the mode of change in microcrack geometry.

3 X-ray CT technique is one of the best methods for non-destructive analysis of rock microstructure. The method established good qualitative correlation between the macroscopic permanent deformation in shale and microscopic changes in the geometry of microcracks.

References

Alejano LR, Alonso E (2005) Considerations of the dilatancy angle in rocks and rock masses. Int J Rock Mech Min Sci 42:481–507

Almisned OA, Al-Quraishi A, Al-Awad MN (2017) Effect of triaxial in situ stress and heterogeneities on absolute permeability of laminated rocks. J Pet Explor Prod Technol 7(2):311–316

Arena A, Piane CD, Sarout J (2014) A new computational approach to cracks quantification from 2D image analysis: application to micro-cracks description in rocks. Comput Geosci 66:106–120

Arganda-Carreras I et al (2017) Trainable Weka Segmentation: a machine learning tool for microscopy pixel classification: Bioinformatics (Oxford Univ Press) Bioinformatics btx 180, PMID 28369169

ASTM (2014) ASTM D7012-14e1: standard test methods for compressive strength and elastic moduli of intact rock core specimens under varying states of stress and temperatures. ASTM International: West Conshohocken, PA

ASTM (2016) ASTM D5731 – 16: standard test method for determination of the point load strength index of rock and application to rock strength classifications. ASTM International: West Conshohocken, PA

ASTM (2019) ASTM D4543-19: Standard practices for preparing rock core as cylindrical test specimens and verifying conformance to dimensional and shape tolerances. ASTM International: West Conshohocken, PA

Batzle ML, Simmons G, Siegfried RW (1980) Microcrack closure in rocks under stress: direct observation. J Geophys Res 85(B12):7072–7090

Bay BK (2008) Methods and applications of digital volume correlation. J Strain Anal Eng Des 43(8):745–760

Bernasconi A (2005) Structural analysis applied to epilepsy. In: Kuzniecky RI, Jackson GD (ed) Magnetic resonance in epilepsy: neuroimaging techniques, 2nd edn. New York, NY, p 464

Bieniawski ZT (1967) Mechanism of brittle failure of rock. Part I: theory of fracture process. Int J Rock Mech Min Sci Geomech Abstr 4(4):395–406

Bobko CP (2008) Assessing the mechanical microstructure of shale by nanoindentation: the link between mineral

composition and mechanical properties. PhD dissertation, Cambridge, Massachusetts Institute of Technology, Massachusetts

Brantut N (2015) Time-dependent recovery of microcrack damage and seismic wave speeds in deformed limestone. J Geophys Res Solid Earth 120:8088–8109

Brooks Z et al (2010) A nanomechanical investigation of the crack tip process zone. In: Proceedings of the 44th U.S. rock mechanics symposium, American Rock Mechanics Association, Alexandria, VA

Budiansky B, O'Connell RJ (1976) Elastic moduli of a cracked solid. Int J Solids Struct 12(2):81–97

Campbell CV (1967) Lamina, laminaset, bed and bedset. Sedimentology 8(1):7–26

Cnudde V, Boone MN (2013) High-resolution X-ray computed tomography in geosciences: a review of the current technology. Earth Sci Rev 123:1–17

Costin LS (1983) Microcrack model for the deformation and failure of brittle rock. J Geophys Res Atmos 88(B11):9485–9492

Crandall D, Moore J, Brown S, Martin K, Mackey P, Paronish T, Carr T, Bowers C (2018) Computed tomography scanning and geophysical measurements of core from the Coldstream 1 MH Well. NETL-TRS-5-2018, NETL Technical Report Series, U.S. Department of Energy, National Energy Technology Laboratory, Morgantown, WV

Cui Z, Han W (2018) In situ scanning electron microscope (SEM) observations of damage and crack growth of shale. Microsc Microanal 24(2):107–115

Cusatis G, Jin C, Li W (2015) Experimental characterization of Marcellus shale. SEGIM Internal Report No. 15-08/478 E. Center for Sustainable Engineering of Geological and Infrastructure Materials, Northwestern University

Deng H, Fitts JP, Peters CA (2016) Quantifying fracture geometry with X-ray tomography: technique of iterative local thresholding (TILT) for 3D image segmentation. Comput Geosci 20:231–244

Ferreira T, Rasband W (2012) ImageJ User Guide–IJ 1.46r, National Institute of Health, Bethesda, MD

Fredrich JT, Di Giovanni AA, Nobel DR (2006) Predicting macroscopic transport properties using microscopic image data. J Geophys Res 111(B3):14

Gnos E et al (2010) Sayh al Uhaymir: a new martian meteorite from the Oman desert. Meteor Planet Sci 37(6):835–854

Griffiths L, Heap MJ, Baud P, Schmittbuhl J (2017) Quantification of microcrack characteristics and implications for stiffness and strength of granite. Int J Rock Mech Min Sci 100:138–150

Guo D et al (2014) Salt and pepper noise removal with noise detection and a patch-based sparse representation. Adv Multimed 2014:14

Gupta N (2019) Fundamental mechanism of time-dependent failure in shale. Graduate theses, dissertations, and problem report, West Virginia University. https://researchrepository.wvu.edu/etd/7445

Gupta N, Mishra B (2017). Creep characterization of Marcellus shale. In: Proceedings of the 51st U.S. rock mechanics symposium, American Rock Mechanics Association, Alexandria, VA, p 4

Gupta N, Das D, Mishra B (2018) Analysis of crack propagation in shale using microscopic imaging techniques. In:

Proceedings of the 52nd US rock mechanics symposium, American Rock Mechanics Association, Alexandria, VA, p 6

Hoek E, Brown ET (1980) Underground excavations in rock. CRC Press, Boca Raton

Jaeger JC, Cook NGW (1976) Fundamentals of rock mechanics. Chapman and Hall, London

Jia L, Chen M, Jin Y (2014) 3D imaging of fracture in carbonate rocks using X-ray computed tomography technology. Carbonate Evaporites 29(2):147–153

Kallu R, Pedram R (2015) Correlations between direct and indirect strength test methods. Int J Min Sci Technol 25(3):355–360

Koeberl C et al (2002) High-resolution X-ray computed tomography of impactites. J Geophys Res 107:19-1–19-9

Kranz RL (1983) Microcracks in rocks: a review. Tectonophysics 100(1–3):449–480

Kuila U et al (2011) Stress anisotropy and velocity anisotropy in low porosity shale. Tectonophysics 503(1–2):34–44

Labuz JF, Shah SP, Dowding CH (1987) The fracture process zone in granite: evidence and effect. Int J Rock Mech Min Sci Geomech Abstr 24(4):235–246

Latief et al (2017) The effect of X-ray micro computed tomography image resolution on flow properties of porous rocks. J Microsc 266(1):69–88

Lenoir N et al (2007) Volumetric digital image correlation applied to X-ray microtromography images from triaxial compression tests on argillaceous rock. Strain 43(3):193–205

Li D, Ngai L, Wong Y (2013) The Brazilian disc test for rock mechanics applications: review and new insights. Rock Mech Rock Eng 46:269–287

Liu B, Wang BS, Ji WG (2001) Closure of micro cracks in rock samples under confining pressure. Chin J Geophys 44(3):419–426

Maire E, Withers PJ (2014) Quantitative X-ray tomography. Int Mater Rev 59(1):1–43

Mark C, Molinda G (2007) Development and application of coal mine roof rating (CMRR) In: Proceedings of the international workshop on rock mass classification in underground mining, NIOSH, Pittsburgh, PA, p 162

Martin CD (1993) The strength of massive Lac du Bonnet granite around underground opening. PhD dissertation, University of Manitoba

Mavko GM, Nur A (1978) The effect of nonelliptical cracks on the compressibility of rocks. J Geophys Res 83(B9):4459–4468

Mogi K (2006) Experimental rock mechanics. CRC Press, London

Mohapatra S (2012) Development and quantitative assessment of a beam-hardening correction model for preclinical micro-CT. MS dissertation, University of Iowa

Molinda G, Mark C (1994) Coal mine roof rating (CMRR): a practical rock mass classification for coal mines. Information circular 9387. U.S. Department of the Interior, Bureau of Mines, Washington, DC

Morgan SP, Einstein HH (2014) The effect of bedding plane orientation on crack propagation and coalescence in shale. In: Proceedings: 48th U.S. rock mechanics symposium, Minneapolis, MN, 1–4 June

Murphy MM (2016) Shale failure mechanics and intervention measures in underground coal mines: results from 50 years of ground control safety research. Rock Mech Rock Eng 49(2):661–671

Niandou H et al (1997) Laboratory investigation of the mechanical behavior of Tournemire shale. Int J Rock Mech Min Sci 34(1):3–16

Nur A, Simmons G (1970) The origin of small cracks in igneous rocks. Int J Rock Mech Min Sci Geomech Abstr 7(3):307–314

O'Connell RJ, Budiansky B (1974) Seismic velocities in dry and saturated cracked solids. J Geophys Res 79(35):5412–5426

Peng SS (2015) Topical areas of research needs in ground control: a state of the art review on coal mine ground control. Int J Min Sci Technol 25(1):1–6

Popova O (2017) Marcellus shale play: geology review. Independent Statistics and Analysis, U.S. Energy Information Administration

Promentilla MAB et al (2009) Quantification of tortuosity in hardened cement paste using synchrotron-based X-ray computed microtomography. Cem Concr Res 39(6):548–557

Rodriguez R et al (2014) Imaging techniques for analyzing shale pores and minerals. U.S. department of energy, national energy technology laboratory, Morgantown, WV

Roen JB (1984) Geology of the Devonian black shales of the Appalachian Basin. Org Geochem 5(4):241–254

Rowe T et al (2001) Forensic palentology: the archaeoraptor forgery. Nature 410:539–540

Schindelin J, Arganda-Carreras I, Frise E et al (2012) FIJI: an open-source platform for biological-image analysis. Nat Methods 9(7):676–682

Sellars E, Vervoort A, Cleyenenbreugel JV (2003) 3D visualization of fractures in rock test samples, simulating deep level mining excavations, using X-ray computed tomography. Geol Soc Lond Spec Public 215:69–80

Simmons G, Richter D (1976) Microcracks in rock. In: Strens RGJ (ed) The physics and chemistry of minerals and rocks. Wiley, New York, pp 105–137

Sprunt E, Brace WF (1974) Direct observation of microcavities in crystalline rocks. Int J Rock Mech Min Sci Geomech Abstr 11:139–150

Tapponnier P, Brace WF (1976) Development of stress-induced microcracks in Westerly granite. Int J Rock Mech Min Sci Geomech Abstr 13:103–112

Voorn M, Exner U, Rath A (2013) Multiscale Hessian fracture filtering for the enhancement and segmentation of narrow fractures in 3D image data. Comput Geosci 57:44–53

Waarsing JH, Day JS, Weinans H (2004) An improved segmentation method for in vivo microCT imaging. J Bone Miner Res 19(10):1640–1650

Wang Q, Song X, Jiang Z (2013) An improved image segmentation method using 3D region growing algorithm. In: Proceedings of the international conference on information science and computer applications, Atlantis Press, Paris, France, p 5

Wu Z, Wong HS, Buenfeld NR (2014) Effect of confining pressure and microcracks on mass transport properties of concrete. Adv Appl Ceram 113(8):485–495

Xradia (2010) MicroXCT-200 and MicroXCT-400 User's guide. Version 7.0, Revision 1.5

Yang X et al (2016) Experimental study of high-temperature fracture propagation in anthracite and destruction of mudstone from coalfield using high-resolution microfocus X-ray computed tomography. Rock Mech Rock Eng 49(9):3723–3734

Zuiderveld K (1994) Contrast Limited adaptive histogram equalization. In: Graphics gems IV, Academic Press Professional Inc., pp 474–485